

# Suppressing Barium Sulfate Crystallization with Hydroxycitrate: A Dual Nucleation and Growth Inhibitor

Ricardo D. Sosa, Xi Geng, Jacinta C. Conrad, Michael A. Reynolds, and Jeffrey D. Rimer\*



Cite This: *Chem. Mater.* 2021, 33, 6997–7007



Read Online

ACCESS |



Metrics & More

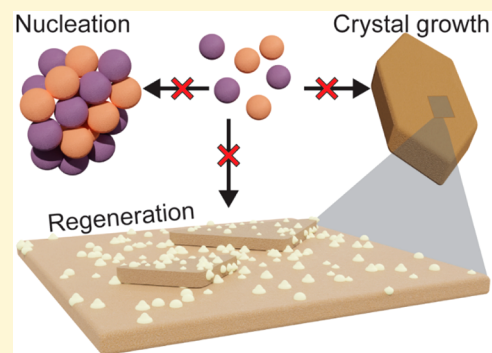


Article Recommendations



Supporting Information

**ABSTRACT:** Designing (macro)molecules that can suppress crystallization is advantageous in natural, pathological, and commercial processes where mineralization has a detrimental impact. Control over this phase transformation is often one-dimensional, meaning that modifiers either block nucleation or impede crystal growth. Inhibitors of mineralization are predominantly composed of either phosphate or carboxylate moieties. It is less common to observe a modifier with only carboxylate functionality inhibit both nucleation and growth. Here, we explore a series of homologous poly(carboxylic acid)s as crystallization inhibitors of barium sulfate (barite), a pervasive and undesirable mineral scale in many industrial processes. Through bulk crystallization, time-resolved microscopy, and scattering measurements, we show that hydroxycitrate (a naturally derived small molecule) effectively inhibits barite nucleation. Moreover, combined microfluidics and atomic force microscopy measurements reveal that hydroxycitrate fully suppresses growth via the formation of a disordered layer on barite surfaces. The rate of barite growth prior to hydroxycitrate exposure could not be recovered over 12 h after removal of the modifier, indicating that growth was sustainably (and irreversibly) altered by exposure to hydroxycitrate. Thus, hydroxycitrate is a barite crystallization modifier capable of suppressing nucleation and irreversibly inhibiting surface growth.



## INTRODUCTION

Crystallization is a ubiquitous phenomenon in natural, biological, and synthetic processes that poses significant problems for pathological or infectious human diseases<sup>1–7</sup> and scale formation in industrial pipelines<sup>8–15</sup> and wellbores.<sup>16</sup> Research efforts to curtail the deleterious effects of mineral precipitation are focused on the development of economical, facile routes to inhibit crystallization. In this study we evaluate additives to inhibit the formation of barium sulfate (barite), which is a persistent inorganic scale component of sparing solubility that forms during energy production.<sup>17–19</sup> One of the most common methods of controlling crystallization is the use of molecular modifiers, which either promote or inhibit rates of crystal nucleation and/or growth.

Nucleation of a crystalline phase is a stochastic process that relies primarily on the supersaturation of the parent solution. Foreign additives can be introduced into growth media as a means of inhibiting crystal nucleation via sequestration of solutes (i.e., reducing supersaturation), disrupting the formation of a critical nucleus (within the context of classical nucleation theory), or altering the self-assembly of clusters that participate in nonclassical mechanisms of crystallization.<sup>20–24</sup> Most common industrial modifiers of the nucleation of barite and other scales are rich in phosphonate moieties (e.g., hydroxyethylidene diphosphonic acid or diethylenetriamine penta(methylene phosphonic acid)).<sup>25–29</sup> Most of these commercial compounds are not readily biodegradable. More-

over, it is difficult to identify (macro)molecules that function as dual inhibitors of crystal growth and nucleation.

Crystal growth modifiers are capable of altering the morphology, size, and/or structure of crystals, often through preferential interaction with different crystallographic facets.<sup>30,31</sup> Modifiers are typically decorated with functional groups (motifs) that have a strong binding affinity to crystal surface sites (kinks, step edges, or terraces) where they impede solute attachment via distinct modes of action<sup>32,33</sup> that alter anisotropic rates of growth with concomitant impact on crystal shape.<sup>30</sup> Citric acid (CA) is a common modifier of numerous minerals, such as calcium oxalate monohydrate and calcium carbonate,<sup>30,34–38</sup> and is an active component in formulations used to prevent pipe corrosion.<sup>39–44</sup> Citrate is also commonly used as a capping agent for materials such as silver (Ag) and gold (Au) nanoparticles to elicit tailored crystal morphologies.<sup>45–47</sup> An analogue of citrate, hydroxycitrate (HCA), has also been found to be an effective inhibitor of calcium-based

Received: June 15, 2021

Revised: August 3, 2021

Published: August 17, 2021



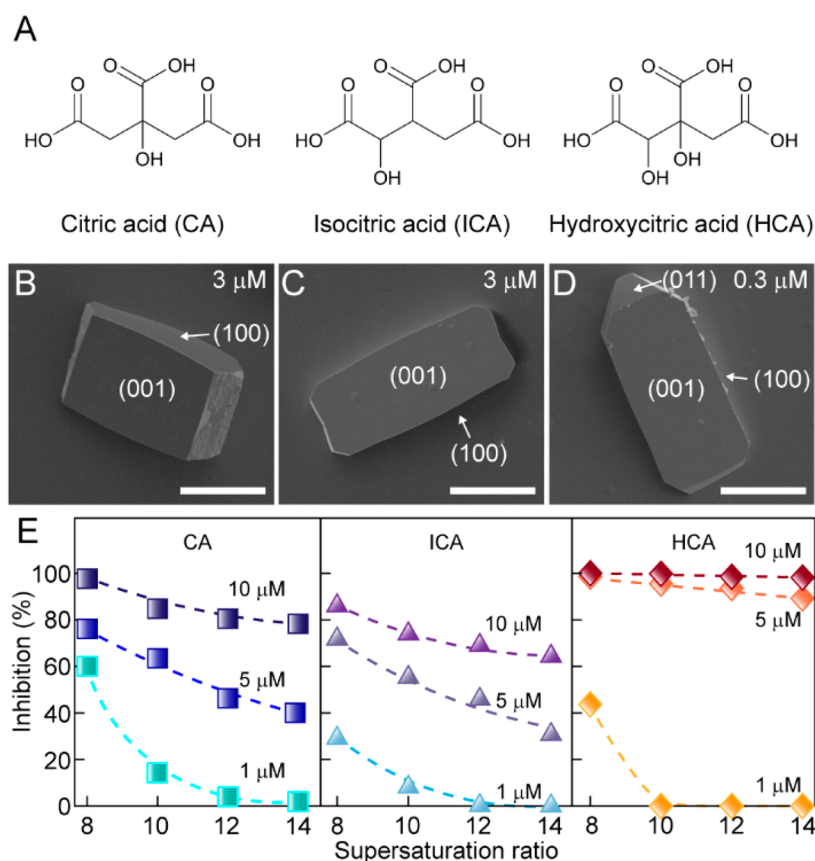


**Figure 1.** (A) Chemical structures of citrate (CA), isocitrate (ICA), and hydroxycitrate (HCA). (B–D) SEM images of representative barite crystals synthesized in the presence of 3  $\mu\text{M}$  CA, 3  $\mu\text{M}$  ICA, and 0.3  $\mu\text{M}$  HCA. Bulk crystallization assays were conducted under quiescent conditions using growth solutions with a supersaturation ratio of 10. Scale bars equal 20  $\mu\text{m}$ . (E) Percent inhibition of barite crystallization as a function of supersaturation ratio in the presence of CA (left), ICA (middle), and HCA (right) at concentrations of 1, 5, and 10  $\mu\text{M}$ , respectively. The percent inhibition was extracted from time-resolved measurements of solution conductivity under continuous stirring. Symbols are the average of at least three separate experiments. Error bars span two standard deviations (those not visible are smaller than the size of the symbols).

crystallization through a unique strain-induced mechanism.<sup>48–52</sup>

Here we implement a cooperative approach to investigate barite crystallization and inhibition pathways across a set of citrate analogues using bulk crystallization assays, microfluidics, and atomic force microscopy. These collective experiments reveal HCA to be the most effective inhibitor among the molecules tested in this study. Through time-resolved microfluidic assays we identified that HCA preferentially binds to barite (010) and (100) facets. Using oblique illumination microscopy (OIM), we investigate barite nucleation events and observe a decrease in barium sulfate particles in the presence of 1 mM HCA, suggesting that HCA acts as a potent barite nucleation inhibitor. Finally, *in situ* AFM studies over a 12 h period of regeneration after exposure of (001) surfaces to HCA reveal a unique mechanism of irreversible barite surface growth inhibition. Together, these studies identify this naturally derived molecule as a dual inhibitor of barite nucleation and growth.

## RESULTS AND DISCUSSION

**Evaluating the Efficacy of Citrate Analogues.** Here we compare three polyprotic acids of similar structure (Figure 1A), citrate (CA), its isomer isocitrate (ICA), and its derivative hydroxycitrate (HCA), owing to their interest as growth inhibitors of inorganic minerals.<sup>7,53</sup> Bulk crystallization assays

were performed in the presence and absence of each modifier using optical and electron microscopy to evaluate changes in crystal size, morphology, and population; and solution conductivity measurements were used to assess crystallization kinetics. For all studies reported herein, the solution pH of the growth medium was adjusted to  $7.1 \pm 0.3$  to evaluate the effects of CA, ICA, and HCA in their fully deprotonated states on barite crystallization (Figure S1). Optical micrographs of glass slides placed at the bottom of crystallization vials were analyzed after 24 h under quiescent conditions to assess the number density of crystals. Our findings reveal that CA has no observable effect on the crystal number density relative to the control (i.e., absence of modifier) within the time of measurement, whereas a monotonic reduction in barite crystal number density is observed with increasing ICA concentration (Figure S2). In contrast, we observed a sharp decline in crystal number density for solutions containing HCA at concentrations above 1.2  $\mu\text{M}$  (Figure S2), which indicates that HCA impedes barite nucleation (as will be discussed later).

Scanning electron microscopy (SEM) images revealed distinct changes in barite crystal morphology with each polyprotic acid. CA produces a barite morphology with a reduced length [010] to width [100] aspect ratio (Figure 1B) compared with that of the control (Figure S3), suggesting a preferential binding that influences the growth along the [010] direction. In media containing ICA, growth is also frustrated

along the [010] direction to yield a distinct crystal habit (Figure 1C and Figure S3). Bulk assays in solutions containing HCA required significantly less modifier to inhibit crystal growth and also resulted in the generation of two uncommon crystal facets: (011) and (010) faces (Figure 1D and Figure S3). The ability of all three modifiers to impart different crystal morphologies is indicative of their unique binding specificities to barite crystal surfaces, consistent with prior studies showing the unique effects of these homologous polyprotic acids as modifiers of other minerals.<sup>6,7,54</sup>

Ionic conductivity has proven to be an effective method of screening the efficacy of crystal growth modifiers by measuring the overall kinetics of crystallization without distinguishing between nucleation and growth. Monotonic reduction in conductivity during the course of crystallization allows for the quantification of the desupersaturation rate (i.e., a surrogate for the kinetic rate of crystallization) in the presence and absence of modifiers (Figure S4). These experiments were performed over a range of barium sulfate supersaturation ( $S = 8-14$ ) to assess the degree to which each modifier inhibits solute depletion over time (reported as a percent inhibition relative to the control) (Figures S5 and S6). The percent inhibition of barite growth for all modifiers generally decreases with increasing supersaturation ratio (Figure 1E), and increasing inhibitor concentration at fixed supersaturation enhances inhibition.

Trends in percent inhibition as a function of supersaturation are nearly identical at  $1 \mu\text{M}$  concentrations of citrate analogues. At concentrations of  $5 \mu\text{M}$ , however, we observe that HCA becomes a significantly more potent crystallization inhibitor. Another unique characteristic of HCA is its ability to completely suppress barite crystallization over the entire range of supersaturation compared to CA and ICA, neither of which exceed 80% inhibition at the highest supersaturation tested.

**Microfluidic Analysis of Barite Growth Inhibition.** We employ a previously developed microfluidic platform<sup>55</sup> to investigate the effects of CA, ICA, and HCA on the macroscopic rates of barite growth in all three principal crystallographic directions. In these experiments, growth solutions are supplied at a constant flow rate to maintain a fixed supersaturation under kinetically controlled growth conditions.<sup>55,56</sup> Optical micrographs taken at periodic time intervals capture the growth of individual barite crystals (Figure 2A and B), wherein it is possible to measure changes in crystal length, width, and thickness owing to orthogonal orientations of seed crystals deposited within the microchannel. In Figure 2C we compare the effects of each modifier on anisotropic rates of barite crystal growth and note the following order of efficacy: HCA > CA  $\approx$  ICA. In the presence of  $5 \mu\text{M}$  CA we observed a 75% reduction in growth rate along the crystal length ( $b$  direction), a 68% reduction of growth along the thickness ( $c$  direction), and virtually no inhibition along the width ( $a$  direction). These results are consistent with quiescent bulk assays (Figure S3) showing CA binding specificity for the barite (010) surface. Microfluidic assays of growth solutions containing ICA reveal similar specificity but lower efficacy (i.e., growth inhibition of 50, 19, and 49% in length, width, and thickness, respectively). Analogous to quiescent bulk assays (Figure 1E), solutions containing  $5 \mu\text{M}$  HCA result in nearly complete inhibition of all crystallographic directions; thus, studies conducted under both quiescent and flow conditions consistently show HCA to be a more potent growth inhibitor.

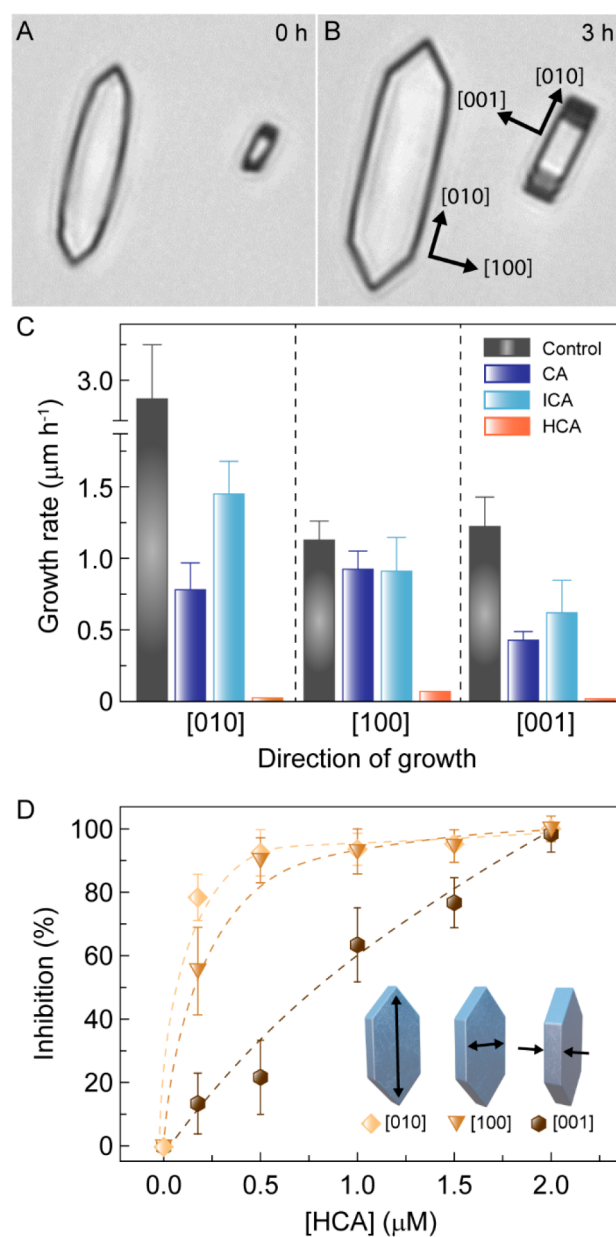


**Figure 2.** Optical micrographs of barite crystals in a microchannel growing under constant flow ( $12 \text{ mL h}^{-1}$ ) of supersaturated solutions ( $S = 7$ ). Images are extracted from Movie S1 at times (A) 0 and (B) 3 h. (C) Growth rate of barite crystals for all three principal crystallographic directions in the absence and presence of  $5 \mu\text{M}$  CA, ICA, and HCA. Data are the average of at least 100 crystals from a single experiment. Error bars equal one standard deviation. (D) Percent inhibition of barite growth in each crystallographic direction obtained from microfluidic assays at different HCA concentrations. Inset: illustrations of barite crystals with indexed length, width, and thickness. Symbols are the average of at least 100 crystals in a single experiment. Error bars span two standard deviations. Dashed lines are interpolated to guide the eye.

The specificity of HCA for barite crystal facets was more clearly differentiated by lowering the modifier concentration below  $2 \mu\text{M}$  (Figure 2D). Under these conditions, we observed that HCA preferentially impedes growth along the [010] and [100] directions (Figure S7) with complete suppression occurring around  $0.5 \mu\text{M}$  HCA. By contrast, HCA's impact on barite growth along the [001] direction is less effective.

Indeed, our study reveals that a fourfold higher concentration of HCA is required to completely suppress growth along the [001] direction. To this end, these results demonstrate that HCA preferentially interacts with barite (010) and (100) surfaces.

#### Hydroxycitrate as a Barite Nucleation Inhibitor.

Having identified HCA as a potent inhibitor of barite growth, we expanded bulk crystallization assays (Figure S3) to systematically assess the effects of HCA on barite nucleation. We conducted OIM measurements under quiescent conditions to track the Brownian motion of particles suspended in liquid. For these studies we compared supersaturated solutions of barium sulfate in the absence and presence of HCA (at fixed supersaturation ratio  $S = 10$ ). In solutions without a modifier, we measured  $65 \pm 6$  particles  $\mu\text{m}^{-2}$  immediately after mixing all components and injecting the sample into the OIM chamber. This observation is consistent with conductivity measurements (Figure S4) where there is an immediate reduction in the ion concentration upon mixing of reagents, which suggests an initial period of rapid precipitation.

In the presence of HCA, OIM measurements revealed a monotonic reduction in particle number density with increasing HCA concentration (Figure 3A). In supersaturated growth solutions containing HCA at concentrations  $\geq 1.75 \mu\text{M}$ , we did not observe particles in the OIM sample chamber, which indicates that HCA functions as an inhibitor of

nucleation. Still frame images from time-resolved OIM measurements revealed that a supersaturated solution ( $S = 10$ ) in the absence of HCA contains large (mostly immobile) particles that have precipitated to the bottom of the sample chamber (Figure 3B). Conversely, a solution with  $3 \mu\text{M}$  HCA contained only trace particles (Figure 3C), consistent with bulk crystallization assays showing the absence of crystals after 24 h (Figure S2).

OIM measurements of barium sulfate solutions at thermodynamic equilibrium (i.e., solubility) and at concentrations below saturation both show no evidence of particles or clusters with sizes that fall within the detection limit of the instrument ( $\geq 20$  nm). As such, there is no evidence to suggest that barite nucleation involves a nonclassical two-step mechanism<sup>57–62</sup> but rather appears to abide by classical nucleation. Interestingly, nucleation can be fully suppressed using only a small quantity of HCA (i.e., 1 mol HCA:250 mol  $\text{Ba}^{2+}$ ). Using a reported potentiometric titration method in the literature<sup>63</sup> to assess ion chelation, there is no appreciable sequestration of free  $\text{Ba}^{2+}$  ions in solution by HCA (Figure S9). This suggests that HCA suppresses barite crystallization not by sequestering solute ions but through processes that disrupt the formation of a critical nucleus.

#### Microscopic Assessment of Barite Growth Inhibition.

*In situ* atomic force microscopy (AFM) has proven to be a valuable technique for probing the dynamics of surface growth and its inhibition at near molecular level. Here, we use *in situ* AFM to compare the modes of action of CA, ICA, and HCA as inhibitors of barite surface growth, focusing on the (001) crystal surface. We selected a supersaturation ( $S = 5.3$ ) within a range previously shown<sup>56</sup> to promote surface growth via two-dimensional birth and spreading. Each single layer has an average height of 3.6 Å (equivalent to a  $c/2$  unit cell dimension) and a triangular morphology bound by [010] and [120] steps (Figure 4A). Step velocity in the [010] direction was measured from sequential images during continuous scanning (Figure 4B). Here we report a relative step velocity  $v/v_0$  where the velocity in the presence of each modifier,  $v$ , is scaled by the value in the absence of modifier,  $v_0$ . Comparison of all three modifiers reveals a similar trend of decreasing relative step velocity with increasing modifier concentration (Figure 4C). Among the molecules tested, HCA is more potent and results in complete suppression of step advancement above  $2 \mu\text{M}$  HCA. Further analysis of the HCA step velocity profile reveals a linear scaling relation between  $v_0(v_0 - v)^{-1}$  and  $c^{-1}$  (where  $c$  is the concentration of the modifier), which is indicative of a kink-blocking mechanism (Figure S11).<sup>1,64</sup> The same analysis for CA and ICA reveals a superlinear scaling relation that seems to suggest a combination of two mechanisms, with the second likely to be that of step pinning (one of the most common mechanisms of surface growth inhibition).<sup>1,3</sup>

Previous examples of kink blockers have shown that layered growth by continuous generation of kink sites at step edges<sup>1</sup> leads to a plateau in the velocity profile (ca. 50% inhibition) with increasing modifier concentration whereby step advancement is not fully suppressed.<sup>2</sup> This result seems to suggest that the mechanism(s) of growth inhibition for all three modifiers in Figure 4C may not be exclusively a kink-blocking or step-pinning mode of action. To test this hypothesis, we also measured the rate of 2D island generation  $J_{2D}$  (number of islands per surface area per time)<sup>65</sup> from time-resolved *in situ* AFM images. Based on reported trends for other crystal

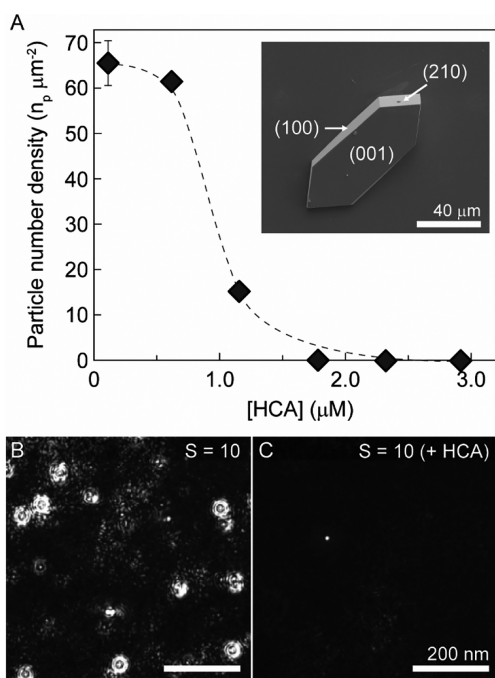


**Figure 3.** Inhibition of barium sulfate nucleation. (A) Number density of barite particles decreasing as a function of HCA concentration in oblique illumination microscopy (OIM) assays. The dashed line is interpolated to guide the eye. Inset: scanning electron micrograph of an unmodified barite crystal displaying three principal facets: (001), (210), and (100). (B and C) OIM images of a supersaturated barium sulfate solution ( $S = 10$ ) in a liquid sample chamber at  $21 \pm 1$  °C. These images were extracted after 30 min of solution preparation from Movies S2 and S3 corresponding to media (B) without modifier and (C) in the presence of  $3 \mu\text{M}$  HCA. Similar experiments with  $5 \mu\text{M}$  CA (Figure S8) resulted in particle formation but with reduced particle number and size compared to those of the control.

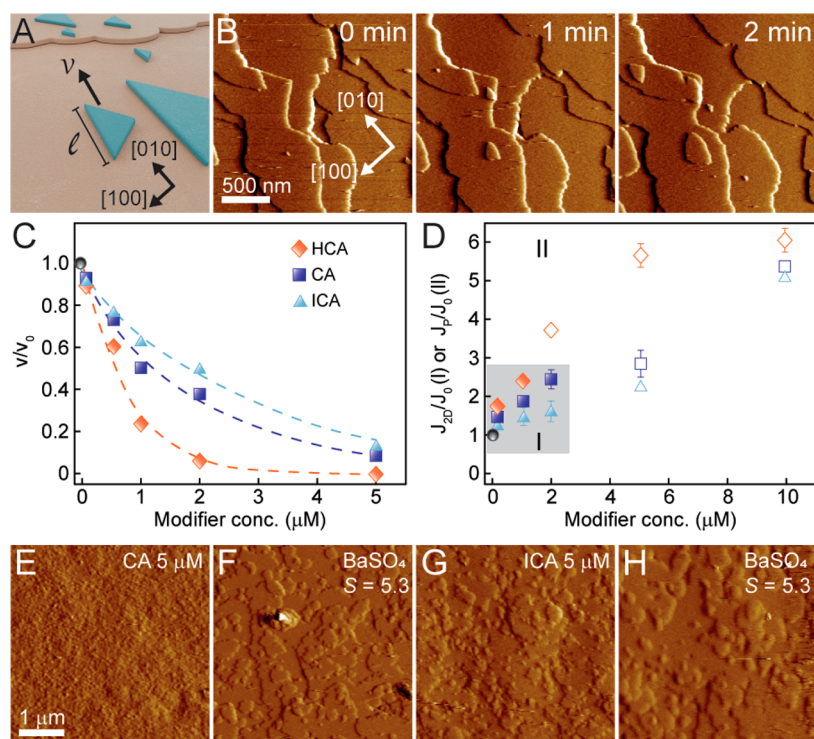


**Figure 4.** Growth and inhibition mechanisms of the barite(001) surface. (A) Idealized schematic of 2D islands on the barite(001) surface illustrating the orientation and length ( $l$ ) of the island in the  $[010]$  direction that is measured over time to calculate step velocity ( $v$ ). (B) Time-resolved *in situ* AFM images extracted from [Movie S4](#) of (001) surface growth under a flow of pure barium sulfate growth solution at a supersaturation ratio of 5.3. (C) Relative step velocity of layers on the (001) barite surface as a function of inhibitor concentration for the  $[010]$  direction of steps. Dashed lines interpolated to guide the eye show the reduction in step velocities owing to inhibitor adsorption on the (001) surface. (D) Rate of 2D particle nucleation of new layers  $J_{2D}$  relative to that in the absence of inhibitors  $J_{2D,0}$  as a function of inhibitor concentration (filled symbols). Light gray region denotes samples in which successive layers correspond to 2D nuclei. In region II, open symbols denote the relative rate of generation  $J_p/J_0$  of surface protrusions with step heights significantly smaller than the barite unit cell dimension ( $c/2$ ). The control in (C) and (D) is indicated by a gray circle. (E) *In situ* AFM image of (001) barite surface growth suppression in the presence of  $5 \mu\text{M}$  CA after 35 min and (F) the recovered surface after reintroducing pure barite growth solution after 55 additional min. (G) *In situ* AFM image of (001) barite surface growth suppression in the presence of  $5 \mu\text{M}$  ICA after 35 min and (H) the recovered surface after reintroducing pure barite growth solution after 55 additional min.

systems,<sup>2</sup> it is expected that the rate of layer generation decreases with increasing modifier concentration owing to the ability of adsorbed modifiers on crystal surfaces to impede the formation of a critical 2D nucleus. Our measurements, however, instead show the opposite trend for all three growth modifiers (Figure 4D) wherein adsorbed modifiers seemingly promote 2D island formation by a mechanism that remains elusive. We report these results as a relative 2D nucleation rate  $J_{2D}/J_{2D,0}$  where measurements in the presence of a modifier are scaled by the value in the absence of a modifier ( $J_{2D,0} = 1.24 \mu\text{m}^{-2} \text{s}^{-1}$ ).

At modifier concentrations below  $2 \mu\text{M}$  (Figure 4D, filled symbols in the shaded gray region I), the rate of 2D nucleation is up to 2.5 times greater than that of the control. Interestingly, concentrations above  $2 \mu\text{M}$  (labeled region II in Figure 4D) lead to further increases in the number of 2D features; however, there are several distinctions between the features observed in regions I and II. First, the 2D features observed in region II neither grow nor dissolve with imaging time. Second, the features in region II have much smaller heights (e.g.,  $1.8 \text{ \AA}$ , Figure S10) compared to the height of a single step ( $3.6 \text{ \AA}$ ) on the barite (001) surface. Although the exact structure of these features cannot be resolved with our measurements, we posit that they are disordered islands (i.e., amorphous or possessing high defect density). The deposition of smaller features

increases with increasing modifier concentration. HCA produces the largest increase in the rate of appearance of surface protrusions, which we label  $J_p$  (Figure 4D, open symbols in region II) to distinguish this phenomenon from layer nucleation  $J_{2D}$ . Time-resolved *in situ* AFM reveals that the (001) surface becomes covered in small features (Figure S12), which suppresses layer advancement once concentrations reach  $5 \mu\text{M}$  for CA (Figure 4E) and ICA (Figure 4G). Experiments were performed to assess potential regeneration of layered growth upon removal of the modifier and reintroduction of fresh (modifier-free) supersaturated growth solution ( $S = 5.3$ ) to the AFM liquid cell. Time-resolved images of barite (001) surfaces reveal that layered growth is recovered to its original value within 1 h for surfaces that had been exposed to CA (Figure 4F) and ICA (Figure 4H); thus, the effects of CA and ICA on barite growth are reversible. In contrast, regeneration of surfaces exposed to  $5 \mu\text{M}$  HCA did not recover rates of layered growth to their original values (i.e., before exposure to HCA) even after 10 h of intermittent AFM imaging, highlighting a mechanism of irreversible growth inhibition.

**Irreversible Inhibition of Barite Growth.** We further investigated the effects of barite (001) surface exposure to HCA as a means of better understanding the mechanism governing irreversible inhibition of layered growth. In the presence of HCA, barite crystal surfaces become laden with

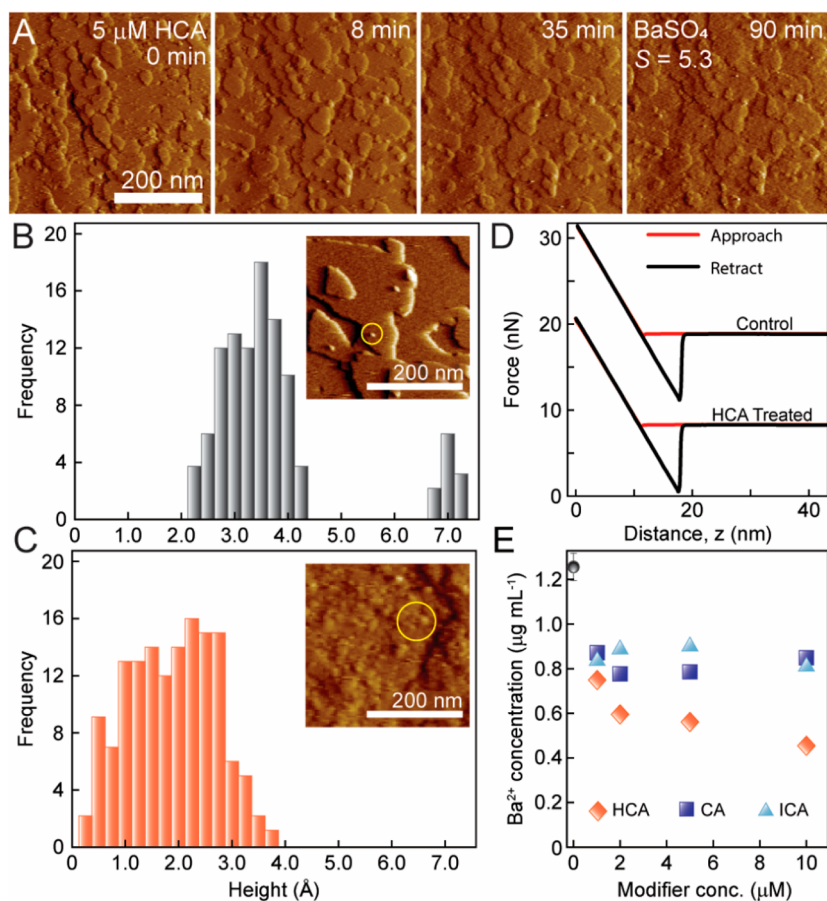


**Figure 5.** (A) Time-elapsing *in situ* AFM images of (001) barite surface growth suppression in the presence of 5  $\mu\text{M}$  HCA after 35 min. Regeneration in fresh growth solution did not reveal surface growth recovery after 55 min of imaging (total 90 min period of inhibition and recovery). (B) Distribution of 2D nuclei height on a (001) barite surface in a supersaturated solution ( $S = 5.3$ ) without any additive. The bimodal distribution corresponds to a large population of single layers (height =  $c/2$ ) and a small number of double layers with heights corresponding to one unit cell. Inset: representative AFM image showing 2D nuclei (yellow circle). (C) Broad distribution of feature heights on a barite (001) surface exposed to a growth solution ( $S = 5.3$ ) containing 5  $\mu\text{M}$  HCA. Inset: representative AFM image showing that these features correspond to protrusions (yellow circle) with heights much smaller than single layers. Distributions of protrusion height in the presence of ICA and CA are provided in Figures S13 and S14, respectively. (D) Chemical force microscopy measurements with a nonfunctionalized AFM tip on a barite surface before (top, control) and after treatment with 5  $\mu\text{M}$  HCA (bottom). Approach (red) and retraction (black) force curves are plotted as a function of distance  $z$  normal to the crystal surface (offset in the  $y$ -axis for clarity). Experiments were performed in supersaturated solution with each curve representing 10 total measurements per sample (each with nearly equivalent profiles). (E) ICP-MS measurements of barium ion concentration in supernatant solutions extracted from dissolution assays under quiescent conditions where  $50 \pm 2$  mg of natural barite was exposed to an undersaturated solution (pH 7) containing different modifier concentrations (note that error bars are smaller than the symbols). The control is indicated by a gray circle.

small features (protrusions) that suppress step advancement. Snapshots from Movie S4 reveal that the layer growth on the barite surface is fully arrested within 8 min of imaging (Figure 5A) with no evidence of continued formation of surface features after 35 min. Attempts to recover surface growth via the introduction of a supersaturated barium sulfate solution resulted in no visible changes to surface features (Figure 5A, 90 min). The experiment was continued over 12 h with a continuous supply of fresh growth solution to the AFM sample cell. After 6 h of intermittent imaging we observed transient features with heights smaller than a single step and modes of feature changes that did not resemble classical island or layered surface growth (Figure S16). After 12 h, we observed only minor changes in surface topography, such as large features with highly corrugated steps resembling a barite growth hillock (Figure S16), and within the time frame of measurement, growth was not restored to its original value before exposure of crystal surfaces to HCA. This sustained (irreversible) growth

inhibition was observed over a range of supersaturation ratios used for AFM ( $S = 5.3$ ) and microfluidics ( $S = 6.5$ , Figure S17) experiments.

Topographical analysis of barite (001) surfaces grown in the absence of a modifier and in the presence of 5  $\mu\text{M}$  HCA revealed distinct differences in the distributions of surface feature heights. Nucleation of islands leads to a population of single layers with a Gaussian distribution centered around a step height of 3.2  $\text{\AA}$  (approximately  $c/2$ ) and a small population of double layers (Figure 5B). The height distribution for protrusions observed on barite surfaces exposed to HCA is much broader, and the average height ( $1.6 \pm 0.8$   $\text{\AA}$ ) is one-half that of the control (Figure 5C and Figure S15). To test whether these small protrusions on barite (001) are either gel- or solidlike in structure, we performed chemical force microscopy (CFM).<sup>66,67</sup> In the CFM experiment, the measured AFM tip-crystal approach and retraction profiles are characteristic of hard surfaces, and there is no

appreciable difference between surfaces exposed to a pure growth solution (Figure 5D, top) and those exposed to HCA (Figure 5D, bottom). For instance, interfaces with soft or gel-like properties exhibit nonlinear profiles,<sup>67</sup> which is not observed in CFM profiles for barite. Thus, this result indicates that the surface features induced by HCA are solidlike.

All three modifiers promote the formation of protrusions on barite crystals to suppress growth; however, this effect is reversible for ICA and CA within a short period of time during regeneration. To quantify the degree of reversibility, we measured the solubility of natural barite crystals in the presence of varying concentrations of HCA, CA, and ICA. A fixed mass of crystals (ca. 50 mg) was placed in an aqueous solution; the crystals dissolved until equilibrium was reached, as determined through measurements of the  $\text{Ba}^{2+}$  ion concentration in the solution over 14 days of incubation at room temperature. In the absence of modifiers (control), saturation occurs around  $1.3 \mu\text{g Ba}^{2+} \text{ mL}^{-1}$  (Figure 5E). Introduction of modifiers decreases the solubility with no apparent trends for increasing concentrations of ICA and CA; however, there is a monotonic reduction in  $\text{Ba}^{2+}$  ion concentration with increasing HCA concentration (orange diamonds in Figure 5E). This result suggests that HCA adsorption on barite surfaces impedes dissolution, leading to an undersaturated (metastable) solution with respect to  $\text{Ba}^{2+}$  ion concentration. Owing to the poor ability of HCA to chelate  $\text{Ba}^{2+}$  ions (Figure S9), the decrease in  $\text{Ba}^{2+}$  availability is attributed to HCA adsorption on barite surfaces. These results are consistent with AFM measurements showing irreversible inhibition of barite (001) surfaces at moderate supersaturation ( $S < 6$ ). In parallel, bulk crystallization and microfluidic assays required higher supersaturation (e.g.,  $S \geq 7$ ) to observe appreciable growth within a reasonable time frame (i.e., order of hours). Under conditions of higher supersaturation, we observed the partial recovery of barite growth (Figure S18) where a regeneration procedure restored growth rates to only 60–70% of their original value prior to exposing barite crystals to HCA. This result indicates sustained 30–40% crystal growth inhibition (relative to the original rate of growth) owing to HCA's irreversible effect on barite crystallization.

## CONCLUSION

In summary, we have compared the performance of citrate and two homologous analogues to assess their relative effect on barite crystallization. Our findings reveal that hydroxycitrate, a molecule differing from the others by the presence of one additional alcohol group, is the most effective crystallization inhibitor with a distinct mode of action relative to citrate and isocitrate. We provide evidence that barite nucleation occurs through a classical mechanism, seemingly in accordance with the Szilard postulate stating that solutes from a supersaturated medium join a nucleus or a growing crystal individually.<sup>68</sup> We also observed that HCA completely suppresses solute assembly into prenucleation clusters, which is surprising given that nucleation is a stochastic process. Indeed, there are few examples of modifiers capable of blocking nucleation. In this study, we showed that HCA also has the ability to fully suppress barite crystal growth. This dual action of crystal nucleation and growth inhibition for a carboxylate-based molecule is uncommon, especially for barite crystallization where we are only aware of one previous example—a recent study by our group showing the macromolecule alginate having similar inhibitory effects on barite nucleation and growth.<sup>56</sup>

The exact mechanism by which HCA suppresses barite crystallization is not fully understood. Specifically, the structure and composition of protrusions that form on the surface of barite crystals in the presence of HCA are unknown. Using AFM, we showed these features are solidlike with heights much smaller than single layers of barite crystals. The fact that these features persist during periods of regeneration to impart sustained (irreversible) inhibition suggests that the crystal lattice is strained, possibly by incorporation of HCA and/or amorphous protrusions into barite crystals. In general, crystal growth regeneration after exposure to a modifier is not widely tested in literature. Furthermore, among the few studies that have conducted regeneration assays,<sup>69</sup> the effects of modifiers tend to be reversible: specifically, the rate of crystal growth is restored to its original value once residual modifier is desorbed from the crystal surfaces.

Factors differentiating whether a modifier has a reversible or irreversible effect on crystallization remain elusive; however, it is evident that the sustained inhibition of crystal growth after removing HCA from the supersaturated medium is a distinct characteristic among known modifiers of barite crystallization. Our findings indicate that HCA is a versatile disruptor of barite crystallization owing to its dual mode of action as a potent inhibitor of nucleation and growth. The ability of HCA to suppress nucleation has the potential to delay scale formation, making this naturally derived compound a promising alternative to commercial compounds used for scale prevention. Moreover, the irreversible action of HCA on the barite crystal growth rate indicates that this modifier may not have to be continuously supplied to the site of scale formation, which can potentially reduce operating costs associated with scale prevention.

## EXPERIMENTAL SECTION

**Materials.** The following reagents were purchased from Sigma-Aldrich: sodium hydroxide (>97%), barium chloride dihydrate (99+%), sodium sulfate (>99%), sodium chloride (>99.5%), sodium citrate tribasic dihydrate ( $\geq 99.0\%$ ), DL-isocitric acid disodium hydrate (93%), potassium hydroxycitrate tribasic monohydrate ( $\geq 95\%$ ), sodium hydroxide (>97%), and hydrochloric acid (37%). Poly-(dimethylsiloxane) (PDMS, Dow Corning SYLGARD 184) was purchased from Essex Brownell. SU-8 2150 photoresist and SU-8 developer were purchased from Kayaku. All chemicals were used as received without further purification. Silicone tubing was purchased from Cole-Parmer. Deionized (DI) water ( $18.2 \text{ M}\Omega\text{-cm}$ ) filtered with an Aqua Solutions RODI-C-12A purification system was used in all experiments.

**Bulk Crystallization Assays.** Barite crystals were synthesized using a protocol established in a previous work.<sup>55</sup> Briefly, aliquots of 10 mM  $\text{BaCl}_{2(\text{aq})}$  and 10 mM  $\text{Na}_2\text{SO}_{4(\text{aq})}$  stock solutions were added into a 20 mL glass vial containing  $\text{NaCl}_{(\text{aq})}$  under mild agitation for 10 s. Samples prepared in the presence of inhibitors were synthesized by adding aliquots of aqueous stock solutions of inhibitors to the synthesis mixture prior to the addition of  $\text{Na}_2\text{SO}_4$ . The reaction mixture produced growth solutions with a total volume of 10 mL, a pH of  $7.1 \pm 0.3$ , and a composition of 0.5 mM  $\text{BaCl}_2$ :0.5 mM  $\text{Na}_2\text{SO}_4$ :600 mM  $\text{NaCl}$ : $x \mu\text{M}$  modifier ( $0 \leq x \leq 5$ ). The sample vials were left undisturbed at  $21 \pm 1 \text{ }^\circ\text{C}$  for 24 h to allow crystallization of hexagonal coffin-shaped barite crystals exhibiting prominent (001), (210), and (100) facets (Figure 3A, inset). Natural barite samples were obtained from Amazon, and the purity was determined as in a previous work.<sup>70</sup>

**Barite Crystallization Kinetics in Bulk Assays.** Conductivity measurements were carried out to assess the crystallization kinetics in the absence and presence of inhibitors under stirred conditions (300 rpm). The conductivity cell (Thermo Scientific Orion DuraProbe)

was vertically immersed into the growth solution, and the readings were recorded by a conductivity meter (Thermo Scientific Orion Star A112 benchtop conductivity meter). The conductivity probe was calibrated with the Orion conductivity standard 100  $\mu\text{S}$  prior to each experiment. A linear fit was performed on the initial linear portion (30 min) of conductivity values over time, which represents the rate of solute consumption and is representative of the rate of crystallization (i.e., both nucleation and growth). Percent inhibition was calculated as % inhibition =  $(1 - \text{RGR}) \times 100\%$ , where RGR represents the relative growth rate, defined as the growth rate in the presence of inhibitors divided by the growth rate in the absence of inhibitors.

**In Situ Microfluidic Assays.** The microfluidic platform used was adapted from a previous work,<sup>55</sup> in which a chip featuring individual straight channels houses barite seed crystals. To generate barite seeds, microchannels were treated with a growth solution at a high enough supersaturation ( $S = 10$ ) to nucleate crystals inside the channels. Microchannels were then flushed thoroughly with 10 mL of DI water at a rate of 120 mL  $\text{h}^{-1}$  to ensure proper adhesion between seed crystals and the microfluidic device substrate. To grow barite crystals without additional nucleation, a growth solution with lower supersaturation ( $S = 7$ ) was delivered into the microchannels using a dual syringe pump (CHEMYX Fusion 200) at a rate of 12 mL  $\text{h}^{-1}$  for 90 min. For growth, two solution components were prepared in individual syringes. One solution contained 0.5 mM  $\text{BaCl}_2$  (aq) and the second solution contained 0.5 mM  $\text{Na}_2\text{SO}_4$  and 1.2 M NaCl. The two solutions were mixed using an inline flow configuration to produce a final composition of 0.35 mM  $\text{BaCl}_2$ , 0.35 mM  $\text{Na}_2\text{SO}_4$ , and 600 mM NaCl. Inhibition studies required the use of two dual syringe pumps, each containing syringes of the same growth solution composition but different quantities of growth modifiers. Time-resolved imaging of barite crystal growth and inhibition using an inverted optical microscope was performed to quantify the kinetics of barite crystallization.

**Materials Characterization and Instrumentation.** Dual star benchtop pH/ISE meters (Orion) equipped with a ROSS Ultra electrode (8102BNUWP) were used for adjusting the pH as well as monitoring pH change during crystallization. Speciation curves were plotted using Hyperquad Simulation and Speciation (HySS2009),<sup>71</sup> with  $\text{p}K_a$  values obtained from literature.<sup>6,72</sup> For *ex situ* microscopy measurements, a clean glass slide ( $0.5 \times 0.5 \text{ cm}^2$ ) was placed at the bottom of the glass vials to collect barite crystals. After crystallization, the glass slide was removed from its solution, thoroughly rinsed with DI water, and dried in air prior to further analysis. Scanning electron microscope (SEM) samples were prepared by attaching carbon tape to SEM studs and subsequently attaching glass slides to carbon tape by gently pressing the glass slide to the tape using tweezers. Scanning electron microscope (SEM) images were obtained on a FEI 235 dual-beam (focused ion-beam) system operated at an accelerating voltage of 15 kV and a working distance of 5 mm. As-synthesized samples were prepared by gently pressing the glass slide containing crystals onto the carbon tape. All samples were coated with a thin layer of gold (ca. 5–10 nm) prior to imaging to minimize charging.

The morphology and size of barite crystals were characterized using a Leica DM2500-M optical microscope in transmittance mode, whereas *in situ* imaging of crystal growth in the microchannels was performed on the Leica DMi8 inverted optical microscope using transmittance mode equipped with HC PL Fluotar 5 $\times$ , 10 $\times$ , 20 $\times$ , and N Plan L 50 $\times$  objectives. At least 15 brightfield images of representative areas on the bottom of the glass vials were captured in transmittance mode for the characterization of crystals grown in the bulk assay. The average [010] length, [100] width, and [001] thickness of barite crystals in optical micrographs were measured from at least 100 crystals per trial and 3 separate trials. For *in situ* time-resolved studies, LAS X software was used to program a minimum of 30 positions along a seeded microchannel, at which images were captured in transmittance mode at 5 min intervals for at least 3 h. Crystals observed *in situ* were analyzed using ImageJ (NIH) using a procedure previously reported.<sup>55</sup> At least 90 crystals located in different channels per batch were analyzed. Crystal dimensions were measured every 5 min during inhibition studies. From the change in

crystal length over time, a growth rate  $r$  was determined for each experimental condition, which can be written as percent inhibition using the relative growth rate described previously.

**Surface Characterization by In Situ Atomic Force Microscopy.** Atomic force microscopy (AFM) was performed to examine the temporal changes in topographical features on the (001) surface of barite. An AFM specimen disk (Ted Pella) covered with a thin layer of thermally curable epoxy (Loctite, China) was placed at the bottom of glass vials during barite synthesis in the bulk assay procedure outlined above. The epoxy was first partially cured in an oven for approximately 6 min at 60  $^\circ\text{C}$  and then dried in air overnight for complete curing. All AFM measurements were performed in a Cypher ES instrument (Asylum Research, Santa Barbara, CA) using silicon nitride probes with a spring constant of 0.08 N  $\text{m}^{-1}$  (Oxford Instruments, PNP-TR 1). The liquid cell (ES-CELL-GAS) contained two ports for inlet and outlet flow to maintain constant supersaturation during AFM measurements. Several concentrations of citrate (CA), isocitrate (ICA), and hydroxycitrate (HCA) ranging from 1 to 10  $\mu\text{M}$  were tested in growth solutions with supersaturation ratio  $S = 5.3$ . The growth solution was delivered to the liquid cell using an in-line mixing configuration in which the two solute solutions ( $\text{Ba}^{2+}$  and  $\text{SO}_4^{2-}$ ) were combined immediately before being introduced into the cell (similar to the microfluidics configuration). Freshly prepared growth solutions were used for each experiment (within 2 h of their preparation). Continuous imaging was performed at ambient temperature in contact mode with a scan rate of 2.44 and 9.77 Hz at 256 lines per scan. For extended time experiments ( $>4$  h), images were taken in contact mode at 30 min intervals. Relative step velocities were determined by measuring the temporal change in 2D island length in the [010] direction for a minimum of 50 2D islands in the presence of inhibitors ( $v$ ) and in the absence of inhibitors ( $v_0$ ).

**Nucleation.** The onset of nucleation and aggregation of particles was characterized by using Nanosight LM10-HS oblique illumination microscopy (OIM) equipped with a green laser (532 nm), which illuminates a thin film of solution at an oblique angle. This method relies on light scattered at wavevectors of order  $\mu\text{m}^{-1}$  and probes length scales in the range  $10^{-3}$ –10  $\mu\text{m}$ . One milliliter samples of supersaturated solution ( $S = 10$ ) in the absence and presence of inhibitors were injected into the OIM chamber, creating a film of thickness 500  $\mu\text{m}$  between two glass substrates, and incubated for varying times at room temperature  $21 \pm 1$   $^\circ\text{C}$ . The average number density of the particles was determined through OIM analysis.<sup>73</sup> A minimum of 10 regions within the liquid film were recorded, and at least 50 particles were analyzed to obtain the particle number density for each inhibitor concentration.

## ■ ASSOCIATED CONTENT

### Supporting Information

The Supporting Information is available free of charge at <https://pubs.acs.org/doi/10.1021/acs.chemmater.1c02060>.

Speciation models for CA, ICA, and HCA as a function of pH, additional bulk crystallization assays for size and number density measurements, data and analysis of ion conductivity measurements, HCA- $\text{Ba}^{2+}$  potentiometric titration curves, additional *in situ* AFM measurements and analysis, additional images and analysis of microfluidic assays, and detailed captions for supporting movies (PDF)

Anisotropic growth of barite seed crystals (AVI)

Time-resolved imaging of a supersaturated barium sulfate solution film using OIM (AVI)

Time-resolved imaging of a supersaturated barium sulfate solution film containing 1.2  $\mu\text{M}$  HCA (AVI)

Time-elapased sequence depicting growth of a (001) barite surface in a supersaturated solution (AVI)

## AUTHOR INFORMATION

## Corresponding Author

Jeffrey D. Rimer – Chemical and Biomolecular Engineering, University of Houston, Houston, Texas 77204, United States; [orcid.org/0000-0002-2296-3428](https://orcid.org/0000-0002-2296-3428); Email: [jrimer@central.uh.edu](mailto:jrimer@central.uh.edu)

## Authors

Ricardo D. Sosa – Chemical and Biomolecular Engineering, University of Houston, Houston, Texas 77204, United States

Xi Geng – Chemical and Biomolecular Engineering, University of Houston, Houston, Texas 77204, United States

Jacinta C. Conrad – Chemical and Biomolecular Engineering, University of Houston, Houston, Texas 77204, United States; [orcid.org/0000-0001-6084-4772](https://orcid.org/0000-0001-6084-4772)

Michael A. Reynolds – Shell Exploration and Production Company, Houston, Texas 77079, United States; [orcid.org/0000-0002-0900-1400](https://orcid.org/0000-0002-0900-1400)

Complete contact information is available at: <https://pubs.acs.org/10.1021/acs.chemmater.1c02060>

## Author Contributions

All authors have given approval to the final version of the manuscript.

## Notes

The authors declare no competing financial interest.

## ACKNOWLEDGMENTS

We acknowledge financial support from Shell Oil Company and the National Science Foundation Graduate Student Fellowship (Award DGE 1144207). J.D.R. and J.C.C. also acknowledge support from the Welch Foundation (Awards E-1794 and E-1869, respectively). We also acknowledge Dr. Wenchuan Ma for help with OIM experiments and analysis.

## REFERENCES

- (1) Olafson, K. N.; Nguyen, T. Q.; Rimer, J. D.; Vekilov, P. G. Antimalarials inhibit hemozoin crystallization by unique drug–surface site interactions. *Proc. Natl. Acad. Sci. U. S. A.* **2017**, *114* (29), 7531–7536.
- (2) Olafson, K. N.; Ketchum, M. A.; Rimer, J. D.; Vekilov, P. G. Mechanisms of hemozoin crystallization and inhibition by the antimalarial drug chloroquine. *Proc. Natl. Acad. Sci. U. S. A.* **2015**, *112* (16), 4946–4951.
- (3) Ma, W.; Lutsko, J. F.; Rimer, J. D.; Vekilov, P. G. Antagonistic cooperativity between crystal growth modifiers. *Nature* **2020**, *577* (7791), 497–501.
- (4) Kim, D.; Olympiou, C.; McCoy, C. P.; Irwin, N. J.; Rimer, J. D. Time-Resolved Dynamics of Struvite Crystallization: Insights from the Macroscopic to Molecular Scale. *Chem. - Eur. J.* **2020**, *26* (16), 3555–3563.
- (5) Kim, D.; Moore, J.; McCoy, C. P.; Irwin, N. J.; Rimer, J. D. Engaging a Battle on Two Fronts: Dual Role of Polyphosphates as Potent Inhibitors of Struvite Nucleation and Crystal Growth. *Chem. Mater.* **2020**, *32* (19), 8672–8682.
- (6) Chung, J.; Taylor, M. G.; Granja, L.; Asplin, J. R.; Mpourmpakis, G.; Rimer, J. D. Factors differentiating the effectiveness of polyprotic acids as inhibitors of calcium oxalate crystallization in kidney stone disease. *Cryst. Growth Des.* **2018**, *18* (9), 5617–5627.
- (7) Chung, J.; Sosa, R.; Rimer, J. D. Elucidating the Effects of Polyprotic Acid Speciation in Calcium Oxalate Crystallization. *Cryst. Growth Des.* **2017**, *17* (8), 4280–4288.
- (8) Abd-El-Khalek, D.; Abd-El-Nabey, B.; Abdel-kawi, M. A.; Ebrahim, S.; Ramadan, S. The inhibition of crystal growth of gypsum

and Barite scales in industrial water systems using green antiscalant. *Water Sci. Technol.: Water Supply* **2019**, *19* (7), 2140–2146.

(9) Bageri, B. S.; Mahmoud, M. A.; Shawabkeh, R. A.; Al-Mutairi, S. H.; Abdurraheem, A. Toward a Complete Removal of Barite (Barium Sulfate BaSO<sub>4</sub>) Scale Using Chelating Agents and Catalysts. *Arabian J. Sci. Eng.* **2017**, *42* (4), 1667–1674.

(10) Bassioni, G. Mechanistic aspects on the influence of inorganic anion adsorption on oilfield scale inhibition by citrate. *J. Pet. Sci. Eng.* **2010**, *70* (3–4), 298–301.

(11) Brown, A.; Merrett, S.; Putnam, J. In *Coil-Tubing Milling/Underreaming of Barium Sulphate Scale and Scale Control in the Forties Field*; Offshore Europe, Society of Petroleum Engineers, 1991.

(12) Bukuaghangin, O.; Neville, A.; Charpentier, T. In *Scale Formation in Multiphase Conditions*, Proceedings of the Oil Field Chemistry Symposium, Gielo, 2015.

(13) Charlesworth, M.; Kalli, C. J.; Thomas, D. G.; Shi, W.; Graham, B. F.; Aman, Z. M.; May, E. F. Compositions and methods for scale inhibition. US 0221849, 2016.

(14) Kenneth Stuart Sorbie, N. L. In *How scale inhibitors work—Mechanisms of selected barium sulphate scale inhibitors across a wide temperature range*, SPE Sixth International Symposium on Oilfield Scale; Exploring the Boundaries of Scale Control, Aberdeen, Scotland, United Kingdom, Aberdeen, Scotland, United Kingdom, 2004.

(15) Mady, M. F.; Bayat, P.; Kelland, M. A. Environmentally-Friendly Phosphonated Polyetheramine Scale Inhibitors-Excellent Calcium Compatibility for Oilfield Applications. *Ind. Eng. Chem. Res.* **2020**, *59* (21), 9808–9818.

(16) Reynolds, M. A. A Technical Playbook for Chemicals and Additives Used in the Hydraulic Fracturing of Shales. *Energy Fuels* **2020**, *34* (12), 15106–15125.

(17) Crabtree, M.; Phil Fletcher, D. E.; Miller, M.; Johnson, A.; King, G. Fighting Scale-Removal and Prevention. *Oilfield Rev.* **1999**, 30–45.

(18) Blount, C. W. Barite solubilities and thermodynamic quantities up to 300 C and 1400 bar. *Am. Mineral.* **1977**, *62*, 942–957.

(19) Abdelgawad, K.; Mahmoud, M.; Elkhatatny, S.; Patil, S. In *Effect of Calcium Carbonate on Barite Solubility Using a Chelating Agent and Converter*, SPE International Conference on Oilfield Chemistry, Society of Petroleum Engineers, 2019.

(20) Van Driessche, A. E. S.; Benning, L. G.; Rodriguez-Blanco, J. D.; Ossorio, M.; Bots, P.; García-Ruiz, J. M. The role and implications of bassanite as a stable precursor phase to gypsum precipitation. *Science* **2012**, *336* (6077), 69–72.

(21) Sommerdijk, N. A. J. M.; With, G. d. Biomimetic CaCO<sub>3</sub> mineralization using Designer Molecules and Interfaces. *Chem. Rev.* **2008**, *108* (11), 4499–4550.

(22) Gower, L. B. Biomimetic Model Systems for Investigating the Amorphous Precursor Pathway and Its Role in Biomineralization. *Chem. Rev.* **2008**, *108* (11), 4551–4627.

(23) Gebauer, D.; Völkel, A.; Cölfen, H. Stable Prenucleation Calcium Carbonate Clusters. *Science* **2008**, *322* (5909), 1819–1822.

(24) Bots, P.; Benning, L. G.; Rodriguez-Blanco, J.-D.; Roncal-Herrero, T.; Shaw, S. Mechanistic Insights into the Crystallization of Amorphous Calcium Carbonate (ACC). *Cryst. Growth Des.* **2012**, *12* (7), 3806–3814.

(25) Pina, C.; Putnis, C. V.; Becker, U.; Biswas, S.; Carroll, E.; Bosbach, D.; Putnis, A. An atomic force microscopy and molecular simulations study of the inhibition of Barite growth by phosphonates. *Surf. Sci.* **2004**, *553* (1–3), 61–74.

(26) Jones, F.; Oliveira, A.; Rohl, A.; Parkinson, G.; Ogden, M.; Reyhani, M. Investigation into the effect of phosphonate inhibitors on barium sulfate precipitation. *J. Cryst. Growth* **2002**, *237*, 424–429.

(27) Coveney, P. V.; Davey, R.; Griffin, J. L.; He, Y.; Hamlin, J. D.; Stackhouse, S.; Whiting, A. A new design strategy for molecular recognition in heterogeneous systems: a universal crystal-face growth inhibitor for barium sulfate. *J. Am. Chem. Soc.* **2000**, *122* (46), 11557–11558.

- (28) Black, S. N.; Bromley, L. A.; Cottier, D.; Davey, R. J.; Dobbs, B.; Rout, J. E. Interactions at the organic/inorganic interface: binding motifs for phosphonates at the surface of Barite crystals. *Journal of the Chemical Society. J. Chem. Soc., Faraday Trans.* **1991**, *87* (20), 3409–3414.
- (29) Baynton, A.; Ogden, M. I.; Raston, C. L.; Jones, F. Barium sulfate crystallization dependence on upper rim calix [4] arene functional groups. *CrystEngComm* **2012**, *14* (3), 1057–1062.
- (30) Grohe, B.; O'Young, J.; Langdon, A.; Karttunen, M.; Goldberg, H. A.; Hunter, G. K. Citrate Modulates Calcium Oxalate Crystal Growth by Face-Specific Interactions. *Cells Tissues Organs* **2011**, *194* (2–4), 176–181.
- (31) Farmanesh, S.; Ramamoorthy, S.; Chung, J.; Asplin, J. R.; Karande, P.; Rimer, J. D. Specificity of growth inhibitors and their cooperative effects in calcium oxalate monohydrate crystallization. *J. Am. Chem. Soc.* **2014**, *136* (1), 367–376.
- (32) Myerson, A. *Handbook of industrial crystallization*; Butterworth-Heinemann: Oxford, U.K., 2002.
- (33) Chernov, A. A. Growth Mechanisms. In *Modern crystallography III*; Springer: New York, 1984; pp 104–158.
- (34) Wierzbicki, A.; Sikes, C. S.; Sallis, J. D.; Madura, J. D.; Stevens, E. D.; Martin, K. L. Scanning electron microscopy and molecular modeling of inhibition of calcium oxalate monohydrate crystal growth by citrate and phosphocitrate. *Calcif. Tissue Int.* **1995**, *56* (4), 297–304.
- (35) Wang, L.; Zhang, W.; Qiu, S. R.; Zachowicz, W. J.; Guan, X.; Tang, R.; Hoyer, J. R.; Yoreo, J. J. D.; Nancollas, G. H. Inhibition of calcium oxalate monohydrate crystallization by the combination of citrate and osteopontin. *J. Cryst. Growth* **2006**, *291* (1), 160–165.
- (36) Tiselius, H.-G.; Fornander, A.-M.; Nilsson, M.-A. The effects of citrate and urine on calcium oxalate crystal aggregation. *Urol. Res.* **1993**, *21* (5), 363–366.
- (37) Qiu, S. R.; Wierzbicki, A.; Orme, C. A.; Cody, A. M.; Hoyer, J. R.; Nancollas, G. H.; Zepeda, S.; De Yoreo, J. J. Molecular modulation of calcium oxalate crystallization by osteopontin and citrate. *Proc. Natl. Acad. Sci. U. S. A.* **2004**, *101* (7), 1811–1815.
- (38) Hess, B.; Zipperle, L.; Jaeger, P. Citrate and calcium effects on Tamm-Horsfall glycoprotein as a modifier of calcium oxalate crystal aggregation. *Am. J. Physiol.* **1993**, *265* (6), F784–F791.
- (39) Zhang, W.; Li, H.-J.; Chen, L.; Sun, J.; Ma, X.; Li, Y.; Liu, C.; Han, X.; Pang, B.; Wu, Y.-C. Performance and mechanism of a composite scaling–corrosion inhibitor used in seawater: 10-Methylacridinium iodide and sodium citrate. *Desalination* **2020**, *486*, 114482.
- (40) Toujas, S.; Vázquez, M.; Valcarce, M. B. Unexpected effect of citrate ions on the corrosion process of carbon steel in alkaline solutions. *Corros. Sci.* **2017**, *128*, 94–99.
- (41) Sobhi, M.; Abdallah, M.; Khairou, K. S. Sildenafil citrate (Viagra) as a corrosion inhibitor for carbon steel in hydrochloric acid solutions. *Monatsh. Chem.* **2012**, *143* (10), 1379–1387.
- (42) Serdaroğlu, G.; Kaya, S.; Touir, R. Eco-friendly sodium gluconate and trisodium citrate inhibitors for low carbon steel in simulated cooling water system: Theoretical study and molecular dynamic simulations. *J. Mol. Liq.* **2020**, *319*, 114108.
- (43) Rachid, T.; Hayat, L. Tri-Sodium Citrate as Corrosion and Scale Inhibitor of Mild Steel in Synthetic Cooling Water System. In *New Challenges and Industrial Applications for Corrosion Prevention and Control*; Younes El, K., Savas, K., Rachid, T., Eds.; IGI Global: Hershey, PA, 2020; pp 16–39.
- (44) Müller, B. Citric acid as corrosion inhibitor for aluminium pigment. *Corros. Sci.* **2004**, *46* (1), 159–167.
- (45) Hajfathalian, M.; Gilroy, K. D.; Hughes, R. A.; Neretina, S. Citrate-Induced Nanocubes: A Re-Examination of the Role of Citrate as a Shape-Directing Capping Agent for Ag-Based Nanostructures. *Small* **2016**, *12* (25), 3444–3452.
- (46) Grys, D.-B.; de Nijs, B.; Salmon, A. R.; Huang, J.; Wang, W.; Chen, W.-H.; Scherman, O. A.; Baumberg, J. J. Citrate Coordination and Bridging of Gold Nanoparticles: The Role of Gold Adatoms in AuNP Aging. *ACS Nano* **2020**, *14* (7), 8689–8696.
- (47) Bastús, N. G.; Comenge, J.; Puentes, V. Kinetically Controlled Seeded Growth Synthesis of Citrate-Stabilized Gold Nanoparticles of up to 200 nm: Size Focusing versus Ostwald Ripening. *Langmuir* **2011**, *27* (17), 11098–11105.
- (48) Liu, X.; Yuan, P.; Sun, X.; Chen, Z. Hydroxycitric Acid Inhibits Renal Calcium Oxalate Deposition by Reducing Oxidative Stress and Inflammation. *Curr. Mol. Med.* **2020**, *20* (7), 527–535.
- (49) Hsu, Y.-C.; Lin, Y.-H.; Shiau, L.-D. Effects of Various Inhibitors on the Nucleation of Calcium Oxalate in Synthetic Urine. *Crystals* **2020**, *10* (4), 333.
- (50) Han, S.; Zhao, C.; Pokhrel, G.; Sun, X.; Chen, Z.; Xu, H. Hydroxycitric Acid Tripotassium Inhibits Calcium Oxalate Crystal Formation in the *Drosophila* Melanogaster Model of Hyperoxaluria. *Med. Sci. Monit.* **2019**, *25*, 3662–3667.
- (51) Chen, W.-C.; Chen, H.-Y.; Lin, W.-Y.; Yang, Y.-R.; Tsai, M.-Y.; Chen, Y.-H. Inhibitory Effect of Hydroxycitrate on Calcium Oxalate Crystal Formation in a *Drosophila* Model. *J. Food Nutr. Res.* **2018**, *6* (11), 706–709.
- (52) Ahmed, A.; Rodgers, A. L.; Elmagbari, F.; Jackson, G. E. In support of hydroxycitrate being clinically investigated as a potential therapy of calcium nephrolithiasis: Theoretical modelling and in vitro investigation of thermodynamic effects. *J. Cryst. Growth* **2021**, *558*, 125956.
- (53) Li, M.; Zhang, J.; Wang, L.; Wang, B.; Putnis, C. V. Mechanisms of Modulation of Calcium Phosphate Pathological Mineralization by Mobile and Immobile Small-Molecule Inhibitors. *J. Phys. Chem. B* **2018**, *122* (5), 1580–1587.
- (54) Chung, J.; Granja, I.; Taylor, M. G.; Mpourmpakis, G.; Asplin, J. R.; Rimer, J. D. Molecular modifiers reveal a mechanism of pathological crystal growth inhibition. *Nature* **2016**, *536* (7617), 446–450.
- (55) Sosa, R. D.; Geng, X.; Reynolds, M. A.; Rimer, J. D.; Conrad, J. C. A microfluidic approach for probing hydrodynamic effects in Barite scale formation. *Lab Chip* **2019**, *19* (9), 1534–1544.
- (56) Geng, X.; Sosa, R. D.; Reynolds, M. A.; Conrad, J. C.; Rimer, J. D. Alginate as a green inhibitor of Barite nucleation and crystal growth. *Mol. Syst. Des. Eng.* **2021**, *6*, 508–519.
- (57) Vekilov, P. G. Nucleation. *Cryst. Growth Des.* **2010**, *10* (12), 5007–5019.
- (58) Vekilov, P. G. The two-step mechanism of nucleation of crystals in solution. *Nanoscale* **2010**, *2* (11), 2346–2357.
- (59) Vekilov, P. G. Dense Liquid Precursor for the Nucleation of Ordered Solid Phases from Solution. *Cryst. Growth Des.* **2004**, *4* (4), 671–685.
- (60) Gebauer, D.; Kellermeier, M.; Gale, J. D.; Bergström, L.; Cölfen, H. Pre-nucleation clusters as solute precursors in crystallisation. *Chem. Soc. Rev.* **2014**, *43* (7), 2348–2371.
- (61) Erdemir, D.; Lee, A. Y.; Myerson, A. S. Nucleation of Crystals from Solution: Classical and Two-Step Models. *Acc. Chem. Res.* **2009**, *42* (5), 621–629.
- (62) De Yoreo, J. J.; Vekilov, P. G. Principles of Crystal Nucleation and Growth. *Rev. Mineral. Geochem.* **2003**, *54* (1), 57–93.
- (63) Thiele, N. A.; MacMillan, S. N.; Wilson, J. J. Rapid Dissolution of BaSO<sub>4</sub> by Macropa, an 18-Membered Macrocyclic with High Affinity for Ba<sup>2+</sup>. *J. Am. Chem. Soc.* **2018**, *140* (49), 17071–17078.
- (64) Bliznakov, G. Adsorption et croissance cristalline. *Ed. CNRS* **1965**, 291–301.
- (65) Markov, I. V. *Crystal Growth for Beginners*, 2nd ed.; World Scientific Press: Hackensack, NJ, 2004; p 564.
- (66) Olafson, K. N.; Clark, R. J.; Vekilov, P. G.; Palmer, J. C.; Rimer, J. D. Structuring of Organic Solvents at Solid Interfaces and Ramifications for Antimalarial Adsorption on  $\beta$ -Hematin Crystals. *ACS Appl. Mater. Interfaces* **2018**, *10* (35), 29288–29298.
- (67) Choudhary, M. K.; Kumar, M.; Rimer, J. D. Regulating Nonclassical Pathways of Silicalite-1 Crystallization through Controlled Evolution of Amorphous Precursors. *Angew. Chem.* **2019**, *131* (44), 15859–15863.
- (68) Gutzow, I. S.; Schmelzer, J. W. P. Kinetics of Crystallization and Segregation: Nucleation in Glass-Forming Systems. In *The*

*Vitreous State: Thermodynamics, Structure, Rheology, and Crystallization*; Springer Berlin Heidelberg: Berlin, Heidelberg, 2013; pp 219–288.

(69) Nene, S. S.; Hunter, G. K.; Goldberg, H. A.; Hutter, J. L. Reversible Inhibition of Calcium Oxalate Monohydrate Growth by an Osteopontin Phosphopeptide. *Langmuir* **2013**, *29* (21), 6287–6295.

(70) Sosa, R. D.; Geng, X.; Agarwal, A.; Palmer, J. C.; Conrad, J. C.; Reynolds, M. A.; Rimer, J. D. Acidic Polysaccharides as Green Alternatives for Barite Scale Dissolution. *ACS Appl. Mater. Interfaces* **2020**, *12* (49), 55434–55443.

(71) Alderighi, L.; Gans, P.; Ienco, A.; Peters, D.; Sabatini, A.; Vacca, A. Hyperquad simulation and speciation (HySS): a utility program for the investigation of equilibria involving soluble and partially soluble species. *Coord. Chem. Rev.* **1999**, *184* (1), 311–318.

(72) Martell, A. E.; Smith, R. M. *Critical stability constants*; Springer: New York, 1974; Vol. 1.

(73) Safari, M. S.; Byington, M. C.; Conrad, J. C.; Vekilov, P. G. Polymorphism of Lysozyme Condensates. *J. Phys. Chem. B* **2017**, *121* (39), 9091–9101.